Journal of Power Sources 428 (2019) 76–81

Contents lists available at ScienceDirect

Journal of Power Sources

journal homepage: www.elsevier.com/locate/jpowsour

Porous amorphous $NiFeO_x$/NiFeP framework with dual electrocatalytic functions for water electrolysis

Fei Hu [a,b,1,**], Yan Zhang [d,1], Xiaochen Shen [a], Jingying Tao [e], Xiaowei Yang [e], Yujie Xiong [c,***], Zhenmeng Peng [a,*]

[a] Department of Chemical and Biomolecular Engineering, University of Akron, Akron, 44325, USA
[b] School of Materials Science and Energy Engineering, Foshan University, Foshan, 528000, PR China
[c] Hefei National Laboratory for Physical Sciences at the Microscale, iChEM (Collaborative Innovation Center of Chemistry for Energy Materials), School of Chemistry and Materials Science, University of Science and Technology of China, Hefei, Anhui, 230026, PR China
[d] Institute for Materials Research Tohoku University, Aobaku, Sendai, 980-8577, Japan
[e] School of Materials Science and Engineering, Tongji University, Shanghai, 201804, PR China

ARTICLE INFO

Keywords:
Water splitting electrocatalyst
Dual function
3D nanoporous framework
Macro-conductivity
Mott-Schottky structure

ABSTRACT

An efficient bulk electrocatalyst is appealing to advance the efficiency of water electrolysis. In this study, we report a function-integrated bulk $NiFeO_x$@NiFeP catalyst that exhibits excellent electrocatalytic activity and stability properties. This new catalyst possesses multiple advantages including three-dimensional (3D) nanoporous framework structure, excellent macro-conductivity, and unique Mott-Schottky architecture, which offers stereochemical and energetic flexibility to interact with reactants with multiple functions including large surface area, fast mass and charge transfers, and favorable catalysis kinetics. The bulk $NiFeO_x$@NiFeP can serve simultaneously as catalyst and current collector, and catalyze both hydrogen evolution reaction (HER) and oxygen evolution reaction (OER), as demonstrated with active and durable overall water splitting performances.

1. Introduction

Sustainable fuel is gradually demanded to resolve the increasing crisis of fossil fuel shortage and environmental pollution. Hydrogen production by electrochemical water splitting is one attractive solution with the mission of replacing noble metal-based catalysts (e.g., Pt, IrO_2, RuO_2) with earth-rich materials and in the meantime achieving high activity and stability for both hydrogen evolution reaction (HER) and oxygen evolution reaction (OER). To date, many transition metal compounds (TMCs) have been reported as promising electrocatalysts for hydrogen production [1–6], among which nickel foam-based bulk structure is considered being applicable in alkaline water splitting electrolyzer. Nanostructured catalysts are intensively studied for water splitting for their outstanding HER [7–9], OER [10–14], and overall water splitting [15–22] performances. Compared to catalysts in nano-powder form, the bulk structure being directly useable as electrodes are advantageous in avoiding the mechanical shedding that might weaken the binding strength of nano-powders to support material and correspondingly cause activity decay. And also, bulk materials have merits as typically exhibited coupling effects and enhanced electron transfer efficiency [23].

We recently developed an amorphous NiFeP bulk material that is exceptionally OER active with overpotentials of only 319 and 540 mV being needed for harvesting 10 mA cm^{-2} current density in alkaline and acid electrolytes, respectively [24]. However, it remained a challenge for the bulk structure to possess a large specific surface area. Intuitively, bottom-down approaches such as selective etching would create three-dimensional (3D) nanostructure channels. 3D nano-architecture electrocatalysts that can be directly used as a current collector has garnered considerable attention because of its structural integrity, for instance, direct bonding, reduced contact resistance, high aspect ratio, abundant surface active sites and sufficient accessibility of reactants and products [25]. Moreover, 3D nano-architectures can provide a superaerophobic surface, which could lower gas bubble size and bubble

* Corresponding author.
** Corresponding author. Department of Chemical and Biomolecular Engineering, University of Akron, Akron, 44325, USA.
*** Corresponding author.
E-mail address: zpeng@uakron.edu (Z. Peng).
[1] These authors contributed equally to this work.

https://doi.org/10.1016/j.jpowsour.2019.04.098
Received 16 January 2019; Received in revised form 19 April 2019; Accepted 24 April 2019
Available online 30 April 2019
0378-7753/

adhesive force by forming a discontinuous triple phase contact line (TPCL) that facilitates gas release and enhances the activity and the stability in gas evolution reactions [26]. Herein, we report the preparation of a 3D nanoporous $NiFeO_x$@NiFeP electrode by selectively etching NiFeP bulk-phase material, and demonstrate the highly-efficient and ultra-stable activity in both HER and OER, evidenced by harvesting 10 mA cm^{-2} current density with a low cell voltage of 1.65 V for over 600-h in 1.0 M NaOH. The outstanding water splitting activity and durability of the $NiFeO_x$@NiFeP catalyst could be attributed to the synergistic effects of 3D nanoporous framework, excellent macro-conductivity, and unique core-shell Mott-Schottky architecture.

2. Experimental

Porous $NiFeO_x$@NiFeP is synthesized using amorphous NiFeP bulk material as precursor. NiFeP long strips, about 5 mm in width and 20 μm in thickness, are obtained by melting spinning NiFeP ingots on a rotating Cu plate in vacuum atmosphere. NiFeP ingots are empirically prepared by melting Fe, Ni, Fe_3P, Ni_3P lumps with scheduled stoichiometric ratio in an electric-arc furnace and then cooling down to the room temperature. The obtained NiFeP long strips are then etched in concentrated H_2SO_4, HNO_3, and HCl acids. The acid concentration is adjusted for achieving an appropriate etching rate in preparing $NiFeO_x$@NiFeP. Specifically, the concentrations of H_2SO_4, HNO_3, and HCl used in this study are 90%, 55%, 90%, respectively. Scanning electronic microscopy (SEM) images and energy dispersive X-ray spectroscopy (EDS) profiles were collected on an FEI Quanata 200 FEG electron microscope operated at 20 kV. High-resolution transmission electron microscopy (HRTEM) images and EDS mapping profiles were obtained on a JEOL JEM-ARM200F Cold-FE high-resolution transmission microscope operated at 200 kV. X-ray diffraction (XRD) patterns were recorded on a Bruker AXS Dimension D8 X-ray diffractometer operating at 40 kV and 35 mA (Cu Kα, $\lambda = 0.154184$ nm). X-ray photoelectron spectrometer (XPS) data were collected on a PHI 5000 Versaprobe II X-ray photoelectron spectrometer. Surface area was measured on Brunauer–Emmett–Teller (BET, ASAP2010, Micromeritics).

The electrocatalytic properties were examined in a three-electrode system on an electrochemical workstation (CHI 760) in an alkaline electrolyte of 1.0 M NaOH aqueous solution or an acid electrolyte of 0.5 M H_2SO_4 aqueous solution. A carbon electrode and an Ag/AgCl electrode were used as counter and reference electrodes, respectively. The Ag/AgCl reference electrode was calibrated using a home-made reversible hydrogen electrode (RHE) by coupling with a Pt wire as a counter electrode. The difference between the Ag/AgCl reference potential and the RHE potential was then corrected. The made porous $NiFeO_x$@NiFeP bulk solid was directly used as a working electrode. Linear scan voltammetry (LSV) was conducted at a scan rate of 1 mVs^{-1} and corrected for iR losses. Electrochemical impedance spectra (EIS) were collected in the frequency range of 100 kHz to 100 mHz with an AC voltage amplitude of 10 mV at potentials of 300 mV versus Ag/AgCl electrode. Cyclic voltammetry (CV) curves were recorded with a sweep rate of 50 mVs^{-1}. Current densities were calculated using geometric surface areas, and electrochemical active surface areas (ECSAs) were estimated by double-layer capacitance measurements. Within ±50 mV versus open-circuit potential (OCP), a series of CVs were conducted at sweep rates of 50–2000 mVs^{-1} to collect the capacitance charging and discharging currents. The currents at the OCP were plotted against the scan rates, whose slopes were used for determining double-layer capacitance of the samples.

3. Results and discussion

Porous $NiFeO_x$@NiFeP (NFPS) is synthesized using amorphous bulk NiFeP (NFP) as starting material. The amorphous feature of the NiFeP is confirmed using HRTEM and XRD characterizations (Figs. S1 and S2a). The elemental mapping (Figs. S1e–f) shows that Ni, Fe and P atoms are homogeneously distributed. Before etching, we perform ab initio molecular dynamics (AIMD) simulations using Vienna ab-initio simulation pack (VASP) for achieving atomic-level insights into the degradation mechanism of amorphous NiFeP and providing an evaluation of the catalyst durability property. A supercell containing 100 atoms is constructed to simulate the amorphous structure, with the electron spins having been taken into account in the simulation. Interactions between individual atoms are described with PAW-PBE type pseudo-potentials on generalized gradient approximation basis. Fig. 1a shows the simulated amorphous $Ni_{40}Fe_{40}P_{20}$ structure, which possesses a system total energy of −671.49 eV. In order to investigate the structural stability, energy deviation from the system total energy by removing individual atoms from the surface is calculated (Fig. 1b). The system exhibits a significant increase when removing Ni, Fe, or P, suggesting unfavored thermodynamics impact on the stability of the amorphous NiFeP. Interestingly, the removal of Fe and Ni atoms causes the biggest and the smallest energy changes (8.93 ± 0.30 eV/Fe atom vs. 6.20 ± 0.24 eV/Ni atom). This indicates that Fe bonds stronger to their neighbor atoms and is more difficult to leach, which is attributed to a stronger Fe—P bond compared to Ni—P bond. Based on these simulation results, it would be expected that the amorphous NiFeP could be selectively etched to create a 3D porous framework.

Porous $NiFeO_x$@NiFeP is synthesized by immersing the amorphous NiFeP bulk in concentrated H_2SO_4, HNO_3, and HCl acids. The obtained products are screened by quantifying the final composition, as being summarized in Table S1. It could be seen that the Ni/Fe ratio remains nearly unchanged when HNO_3 and HCl etchant solutions are used. In contrast, the Ni/Fe ratio decreases with use of H_2SO_4 solution. By varying the H_2SO_4 concentration, bath temperature and etching time, the elemental contents in the final products are varied as shown in Tables S2–S4. Ni seems preferentially dissolved when the H_2SO_4 concentration is higher than 70% and the bath temperature is higher than 70 °C, which is consistent with the AIMD simulations. With an increase in the etching time, the oxygen percentage and Ni/Fe ratio firstly increase and then decrease, inferring a trade-off between nickel dissolution and pore creation. The highest porosity is obtained when the $Ni_{40}Fe_{40}P_{20}$ is etched for 12 h (Fig. S3), evidenced by an 11.8 fold increase in the ECSA value compared to the pristine precursor. N_2 adsorption-desorption measurement further confirms that the resulting sample exhibits a Brunauer–Emmett–Teller (BET) surface area of 13.27 m^2/g with an average nanopore size of 6.94 nm (Fig. S4 and Table S5).

The obtained porous $NiFeO_x$@NiFeP well maintains the amorphous feature, evidenced by the XRD pattern (Fig. S2b) and selected area electron diffraction (SAED, Fig. 2a). The porous structure is characterized using HRTEM. A ~500 nm thick layer consisting of intertwined nanostructured scaffolds on the top of solid NiFeP substrate is observed in Fig. 2a. This top layer shows a significantly lower image contrast compared with the NiFeP substrate, owing to the porous characteristic and likely a composition change. Some mesopores are also observed, which would facilitate efficient mass transfer by creating transport channels and lowering down the transport resistance. Fig. 2b–c presents a nanoporous framework with pore diameters of 20–25 nm. The EDS mapping in Fig. 2d further confirms the core-shell structure. The shell is about 2–10 nm in thickness and composes of Ni, Fe, O, and a trace of P and S, evidenced by the detection of these elements using EDS in Fig. S8e. Similar structures have been reported by chemical dealloying on Pt—Cu and Pt—Co alloys [27]. We term this unique structure as $NiFeO_x$@NiFeP framework. We disrupt the top nanoporous layer from the NiFeP substrate, and carefully characterize these porous and amorphous structures using TEM (Fig. S5). It is critical to note that the porous NiFeP framework stands a great chance to achieve exceptional activity and durability properties. The structural amorphousness creates dense under-coordinated surface sites that would offer energetic flexibility to interact with reactants. The metallic skeleton would endow excellent electrical conductivity for efficient electron transfer between the NiFeP

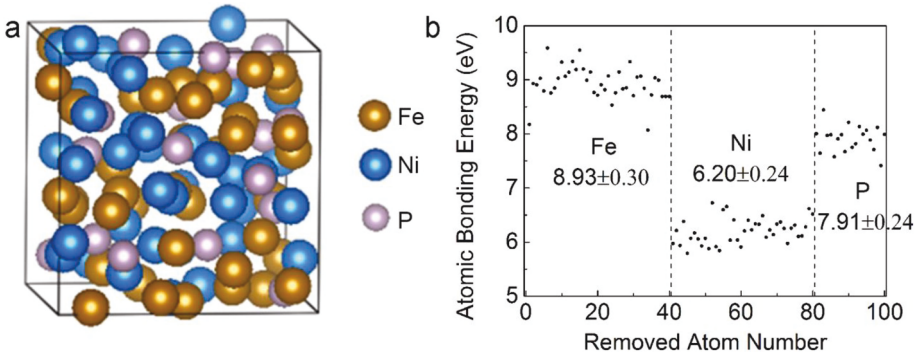

Fig. 1. (a) Supercell image illustrating the $Ni_{40}Fe_{40}P_{20}$ amorphous structure and (b) changes in average bonding energy caused by removal of individual atoms from the amorphous structure.

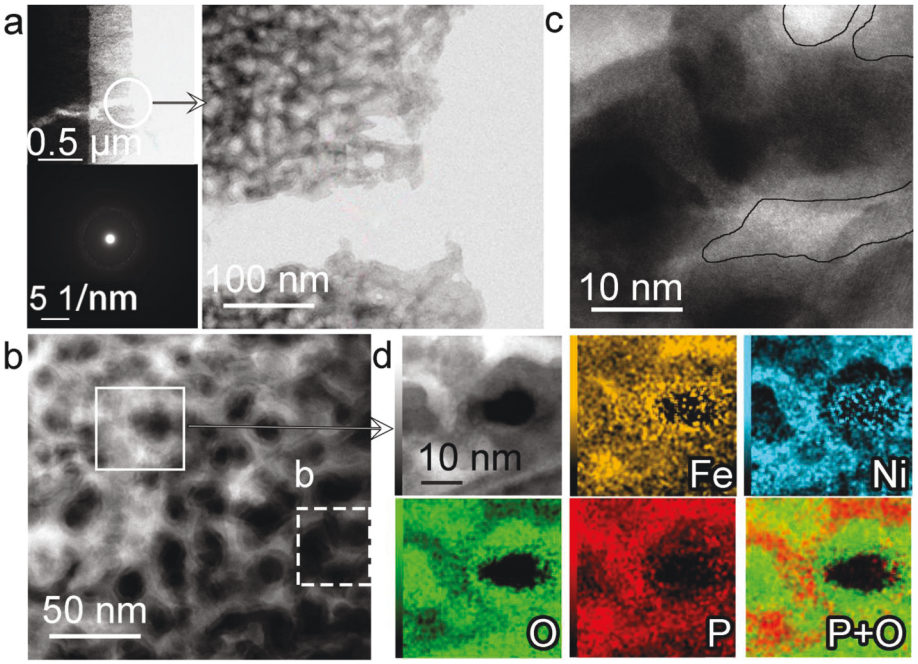

Fig. 2. (a) TEM image and SAED pattern of the $NiFeO_x$@NiFeP framework demonstrating an amorphous porous feature, (b, c) HRTEM showing the nanoporous scaffold, and (d) EDS mapping confirming a core-shell structure.

skeleton and surface active sites in the ultrathin $NiFeO_x$ skin, which further prevents the metallic core from degradation [28]. These features, together with a large active surface area resultant of the porous structure, are expected to significantly improve the reaction activity and structural stablity.

Upon acquiring the structural information, it is imperative to understand the chemical environment information of the $NiFeO_x$@NiFeP framework. The XPS reveals the presence of Ni, Fe, P, S, and O elements from the complete survey spectrum in Fig. 3a. In Fig. 3(b and c), the high-resolution Ni 2p and Fe 2p XPS can be deconvoluted into metallic states at peaks 853.2 eV (Fe—Fe) and 707.6 eV (Ni—Ni) respectively. The peaks at around 856.0 and 874.0 eV along with two satellite peaks at 861.4 and 879.7 eV are well fitted with Ni 2p3/2 and Ni 2p1/2 of the oxidized nickel. The peaks located at 711.4 and 723.9 eV and their corresponding shakeup resonance at 719.8 eV represent Fe 2p3/2 and Fe 2p1/2 in the oxidation state of iron, which is in agreement with the TEM observations. The P 2p spectrum in Fig. 3d can be deconvoluted into three peaks at 133.0, 129.8 and 128.9 eV. The two peaks with lower binding energy are ascribed to that of metal phosphide, and the third peak is designated to phosphate, respectively. The high resolution spectrum of S 2p in Fig. 3e shows two peaks centered at 162.9 and 161.7 eV that could be assigned to S $2p_{1/2}$ and S $2p_{3/2}$, respectively. The peak at 164.1 eV is attributed to metal-sulfur bond [29]. For the O 1s XPS spectra in Fig. 3f, the peak at 531.5 eV is assigned to phosphate and hydroxyl species, and the peaks at about 530.5 and 532.2 eV are attributed to metal-O bond and absorbed O_2, respectively.

The $NiFeO_x$@NiFeP framework is then evaluated for the electrocatalytic properties in water electrolysis. Fig. 4a and Figs. S6a–b show the OER and the HER LSV curves in 1.0 M NaOH. A current density of 10 mA cm^{-2} is achieved with an overpotential of only 210 mV for OER and an overpotential of only 180 mV for HER, respectively. The Tafel slopes of 37.0 and 85.2 mV·dec^{-1} demonstrate favorable kinetic processes for OER and HER, respectively. In an acid electrolyte of 0.5 M H_2SO_4 solution, the $NiFeO_x$@NiFeP electrodes gain a current density of 10 mA cm^{-2} at 680 mV for OER and 100 mV overpotential for HER, respectively (Fig. 4b and Figs. S6c–d). Their corresponding Tafel slopes are 94.0 and 67.2 mV·dec^{-1}. The overpotential and Tafel slope are smaller than the documented NiFe-based catalysts in literature, indicating outstanding activity of the $NiFeO_x$@NiFeP in this study [30–34]. The XPS spectra in Fig. 3 further indicate that the HER and the OER have different active sites for water splitting, as obvious appearance of metallic Fe—Fe and Ni—Ni bonds are witnessed after HER

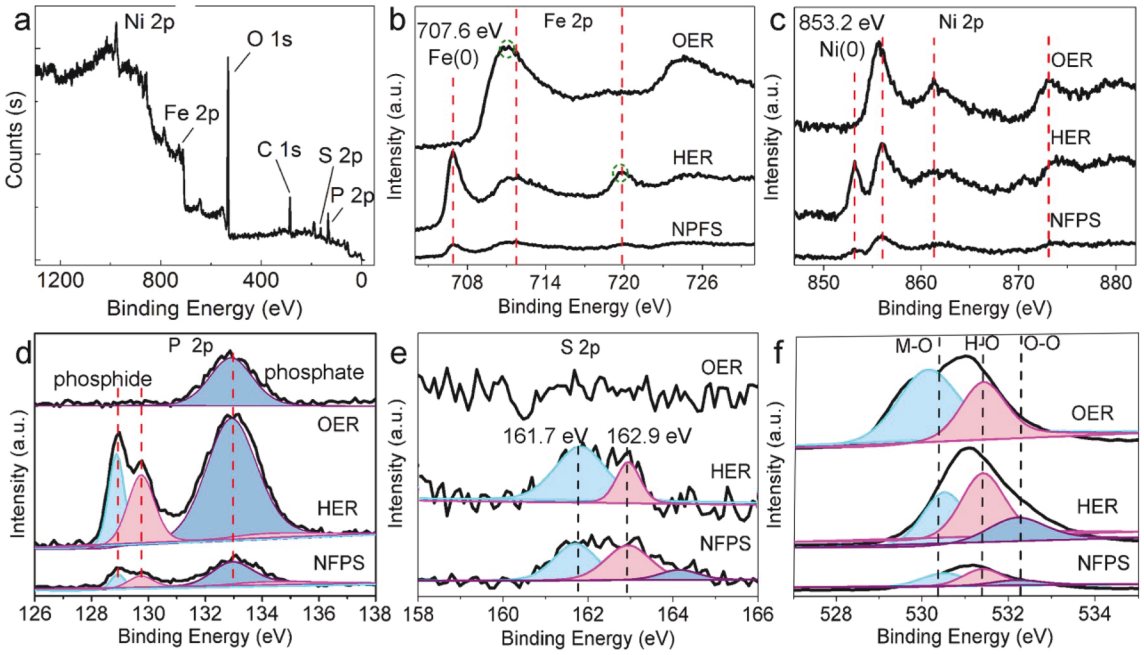

Fig. 3. (a) Full survey spectrum and high-resolution XPS spectra of (b) Fe 2p, (c) Ni 2p, (d) P 2p, (e) S 2p, and (f) O 1s of as-prepared $NiFeO_x$@NiFeP framework and after OER and HER tests.

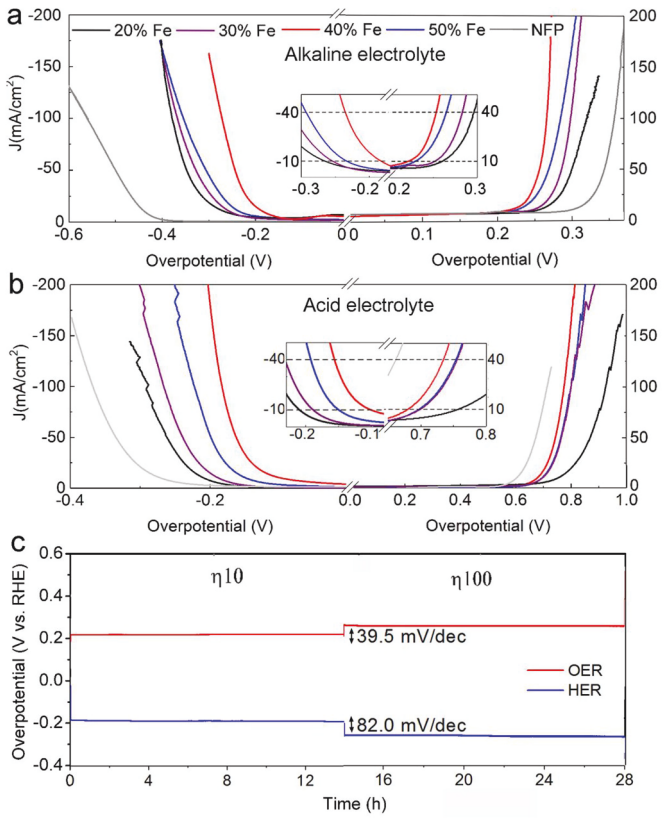

Fig. 4. Polarization curves of the $NiFeO_x$/NiFeP framework in the (a) 1.0 M NaOH, and (b) 0.5-M H_2SO_4 solution. The inset diamgram of panel (a–b) shows the overpotentials at 10 mA cm^{-2}. (c) the stability of the $NiFeO_x$/NiFeP framework in the 1.0 M NaOH at current densities of 10 and 100 mA cm^{-2}.

(Fig. 3a–b) and noticeable disappearance in non-metallic P and B occurs after OER (Fig. 3d–e). The XPS spectra of O 1s further prove that a higher percentage of M – O bond than H—O bond is generated after OER (Fig. 3f), representing in OER the active sites are (hydro)xide rather borides or phosphides.

We also conduct XPS on the $NiFeO_x$@NiFeP framework after OER in a 0.5 M H_2SO_4 electrolyte, as shown in Fig. S7. It is observed that the XPS spectra for Fe, Ni, P, and S are similar to the sample after HER, which indicates that the acidic media is more influenced for the outer oxides skin as severe dissolution might occur. To validate the hypothesis, we compare the surface morphology of the $NiFeO_x$@NiFeP framework before and after OER in the 0.5 M H_2SO_4 electrolyte, as shown in Fig. S8. Larger and more uniform nanopores and microcracks are observed after OER, inferring sample dissolution happens during OER. Fig. S8e shows close percentages of elements Ni, Fe, P, S except O for samples before and after OER in an acidic solution. It is speculated that the dissolution rate is faster than the oxide formation rate, resulting in inferior stability and the degradation of electrocatalysts in acidic media.

The stability of the $NiFeO_x$/NiFeP framework in the alkaline electrolyte is carefully examined. Under the chronovoltametry testing condition, low overpotentials of 220 and 200 mV are needed for OER and HER to achieve 10 mA·cm^{-2}current density, respectively. Only slight increases in the overpotential (39.5 and 82.0 mV) would reach 100 mA cm^{-2}, which is in good agreement with the Tafel slopes in Fig. S6. The superior dual-functional HER and OER performance enlighten us to test its overall water splitting efficiency. In 1.0 M NaOH electrolyte, the water electrolysis could achieve 10 mA cm^{-2} current density with 1.65 V cell voltage and be maintained for at least 600-h, as shown in Fig. 5a. This performance using the $NiFeO_x$/NiFeP electrodes is significantly improved compared to other tested electrode materials including RuO_2/Pt, Pt/Pt, and NiFeP/NiFeP (the insert of Fig. 5a) and many other reported catalyst materials (Table S6).

The outstanding activity and durability of the 3D nanoporous $NiFeO_x$@NiFeP can be attributed to its unique integrated functions [35]. First of all, the metallic NiFeP skeleton has the virtue of providing fast electron flow and minimizing the potential gradient between the current collector and active sites. The electrical conductivity of the $NiFeO_x$@-NiFeP electrode is 923.60 S/cm as measured by a four-point tester, which is slightly lower than the untreated NiFeP of 936.18 S/cm. Fig. 5b shows a smaller EIS semicircle diameter in the high frequency as compared to NiFeP, confirming much lower interface charge-transfer

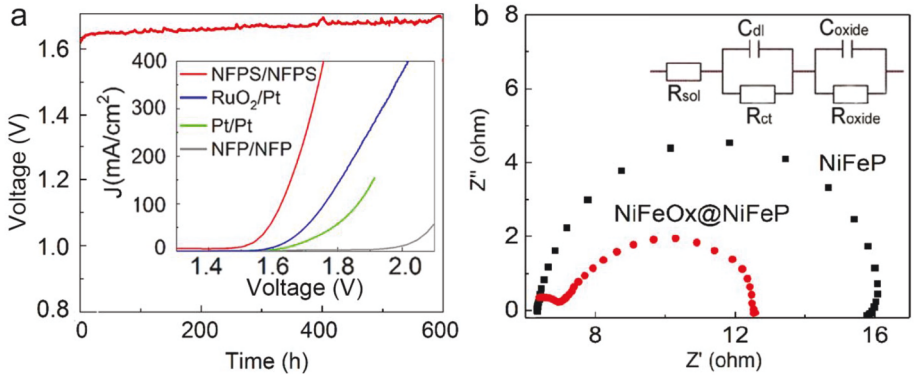

Figure 5. (a) Overall water splitting stability of the $NiFeO_x$@NiFeP framework (NFPS) electrodes operating at 10 mA cm^{-2} for 600-h and overall water splitting LSV (inset figure), (b) EIS spectra of the $NiFeO_x$@NiFeP framework and NiFeP and an equivalent circuit model for the EIS spectra (inset figure).

resistance and correspondingly fast reaction kinetics. Accordingly, we anneal the $NiFeO_x$@NiFeP electrode at temperatures of 200–500 °C for 1 h in Ar atmosphere. Fig. S9 validates a gradual deterioration of the electrochemical activity due to the loss of marco-conductivity, and the sample loses its activity when it is annealed at 500 °C.

Secondly, the core-shell structure would also benefit the electrochemical activity with the lattice strain and the Mott-Schottky effect as compared to pure oxide catalysts [19,36,37]. The outer oxide shell $NiFeO_x$ is typically semiconducting, with the work function being dramatically lower than that of metallic NiFeP. Thus in the $NiFeO_x$@NiFeP structure, electrons flow through the metal/semiconductor interface due to the Mott-Schottky effect until the work function equilibrium is reached. The redistribution of electrons at the $NiFeO_x$@NiFeP interface results in band bending, pulling down the valence band of $NiFeO_x$. The electron redistribution at the $NiFeO_x$@NiFeP interface can be directly demonstrated by the XPS analysis results (Fig. 3). A shift of the Ni 2p from 711.4 eV to 711.3 eV and 711.0 eV occurs after OER and HER, respectively. In the meantime, the Fe 2p peaks shift from 856.0 eV to 856.2 eV and 855.8 eV, respectively, representing the rectifying contact at the $NiFeO_x$/NiFeP interface. The work function of $NiFeO_x$ shell is thus lowered with obviously improved activity, which largely depends on electron donating ability of electrocatalyst to reactant molecules.

The durability of a catalyst is indicative of a permanent lifetime of an electrolyzer. The function-integrated structure of the $NiFeO_x$@NiFeP exhibits the outstanding long-term durability because the amorphous oxide shell is reactive inact in alkaline media but electrochemical active with electrons. A fast charge transfer avoids the accumulation of electrons in the solid/oxide/liquid interface. The oxide skin preventing penetrative oxidation of the metallic core, which in turn maintains the function-integrated structure and avoids structural degradation.

4. Conclusions

In summary, porous amorphous $NiFeO_x$@NiFeP catalyst that is highly active and durable in both HER and OER is obtained, benefiting from the synergic functional-structural effects. The direct bonding of $NiFeO_x$ active sites on etched 3D nanostructure channels offers sufficient surface area. The continuous electrically conductive framework promises a quick charge supply and short ion diffusion distance. Moreover, the under-coordinated oxide surface and the Mott-Schottky interface enhance the electronic configuration and assure fast catalysis kinetics. The $NiFeO_x$@NiFeP shows highly-efficient and ultra-stable overall water splitting activity, with a current density of 10 mA cm^{-2} being harvested at a cell voltage of 1.65 V for over 600-h in 1.0 M NaOH electrolyte. This work directs a way for bulk materials to gain a remarkable electrocatalytic activity and durability, and offers a better alteration to dramatically boost the efficiency of alkaline water splitting electrolyzer.

Acknowledgment

We acknowledge financial support from the University of Akron and NSF (CHE-1665265). Y.X. was supported by NSFC (21573212, U1532135, 21725102). F. Hu was supported by NSFC (21802103).

Appendix A. Supplementary data

Supplementary data to this article can be found online at https://doi.org/10.1016/j.jpowsour.2019.04.098.

References

[1] X. Long, J. Li, S. Xiao, K. Yan, Z. Wang, H. Chen, S. Yang, A strongly coupled graphene and FeNi double hydroxide hybrid as an excellent electrocatalyst for the oxygen evolution reaction, Angew. Chem. Int. Ed. 53 (2014) 7584–7588.
[2] Z. Zeng, K.-C. Chang, J. Kubal, N.M. Markovic, J. Greeley, Stabilization of ultrathin (hydroxy)oxide films on transition metal substrates for electrochemical energy conversion, Nat. Energy 2 (2017) 17070.
[3] B.J. Trzesniewski, O. Diaz-Morales, D.A. Vermaas, A. Longo, W. Bras, M.T. Koper, W.A. Smith, In situ observation of active oxygen species in Fe-containing Ni-based oxygen evolution catalysts: the effect of pH on electrochemical activity, J. Am. Chem. Soc. 137 (2015) 15112–15121.
[4] M. Gong, Y. Li, H. Wang, Y. Liang, J.Z. Wu, J. Zhou, J. Wang, T. Regier, F. Wei, H. Dai, An advanced Ni-Fe layered double hydroxide electrocatalyst for water oxidation, J. Am. Chem. Soc. 135 (2013) 8452–8455.
[5] M.-I. Jamesh, X. Sun, Recent progress on earth abundant electrocatalysts for oxygen evolution reaction (OER) in alkaline medium to achieve efficient water splitting – a review, J. Power Sources 400 (2018) 31–68.
[6] M.-I. Jamesh, X. Sun, Recent progress on earth abundant electrocatalysts for hydrogen evolution reaction (HER) in alkaline medium to achieve efficient water splitting –A review, J. Nat. Gas Chem. 34 (2019) 111–160.
[7] X.F. Lu, L. Yu, X.W. Lou, Highly crystalline Ni-doped FeP/carbon hollow nanorods as all-pH efficient and durable hydrogen evolving electrocatalysts, Sci. Adv. 5 (2019) eaav6009.
[8] J.-X. Feng, S.-Y. Tong, Y.-X. Tong, G.-R. Li, Pt-like hydrogen evolution electrocatalysis on PANI/CoP hybrid nanowires by weakening the shackles of hydrogen ions on the surfaces of catalysts, J. Am. Chem. Soc. 140 (2018) 5118.
[9] R. Ye, P. del Angel-Vicente, Y. Liu, M.J. na Arellano-Jimenez, Z. Peng, T. Wang, Y. Li, B.I. Yakobson, S.-H. Wei, M.J. Yacaman, J.M. Tour, High-Performance hydrogen evolution from $MoS_{2(1-x)}P_x$ solid solution, Adv. Mater. 28 (2016) 1427–1432.
[10] P. He, X.-Y. Yu, X.W. Lou, Carbon incorporated Ni-Co mixed metal phosphides nanoboxes with enhanced electrocatalytic activity for oxygen evolution, Angew. Chem. Int. Ed. 56 (2017) 3897.
[11] X. Wang, L. Yu, B.Y. Guan, S.Y. Song, X.W. Lou, Metal-organic framework hybrid-assisted formation of Co_3O_4/Co-Fe oxide double-shelled nanoboxes for enhanced oxygen evolution, Adv. Mater. 30 (2018), 1801211.
[12] B. Konkena, J. Masa, A.J.R. Botz, I. Sinev, W. Xia, J. Koßmann, R. Drautz, M. Muhler, W. Schuhmann, Metallic $NiPS_3$@NiOOH core-shell heterostructures as highly efficient and stable electrocatalyst for the oxygen evolution reaction, ACS Catal. 7 (2017) 229–237.
[13] H. Liang, A.N. Gandi, D.H. Anjum, X. Wang, U. Schwingenschlögl, H.N. Alshareef, Plasma-assisted synthesis of NiCoP for efficient overall water splitting, Nano Lett. 16 (2016) 7718–7725.
[14] L.A. Stern, L. Feng, F. Song, X. Hu, Ni_2P as a Janus catalyst for water splitting: the oxygen evolution activity of Ni_2P nanoparticles, Energy Environ. Sci. 8 (2015) 2347–2351.

[15] E. Hu, Y. Feng, J. Nai, D. Zhao, Y. Hu, X.W. Lou, Construction of hierarchical Ni–Co–P hollow nanobricks with oriented nanosheets for efficient overall water splitting, Energy Environ. Sci. 11 (2018) 872–880.
[16] W. Zhu, W. Zhang, Y. Li, Z. Yue, M. Ren, Y. Zhang, N.M. Salehb, J. Wang, Energy-efficient 1.67 V single-and 0.90 V dual-electrolyte based overall water-electrolysis devices enabled by a ZIF-L derived acid-base bifunctional cobalt phosphide nanoarray, J. Mater. Chem. 6 (2018) 24277.
[17] H. Jia, R. Jiang, W. Lu, Q. Ruan, J. Wang, J.C. Yu, Aerosol-spray metal phosphide microspheres with bifunctional electrocatalytic properties for water splitting, J. Mater. Chem. 6 (2018) 4783–4792.
[18] M. Ledendecker, S.K. Calderón, C. Papp, H. Steinrück, M. Antonietti, M. Shalom, The synthesis of nanostructured Ni_5P_4 films and their use as a non-noble bifunctional electrocatalyst for full water splitting, Angew. Chem. 127 (2015) 12538.
[19] Z.-H. Xue, H. Su, Q.-Y. Yu, B. Zhang, H.-H. Wang, X.-H. Li, J.-S. Chen, Janus Co/CoP nanoparticles as efficient Mott-Schottky electrocatalysts for overall water splitting in wide pH range, Adv. Energy Mater 7 (2017), 1602355.
[20] B. Song, K. Li, Y. Yin, T. Wu, L. Dang, M. Cabán-Acevedo, J. Han, T. Gao, X. Wang, Z. Zhang, J.R. Schmidt, P. Xu, S. Jin, Tuning mixed nickel iron phosphosulfide nanosheet electrocatalysts for enhanced hydrogen and oxygen evolution, ACS Catal. 7 (2017) 8549–8557.
[21] Z. Dai, H. Geng, J. Wang, Y. Luo, B. Li, Y. Zong, J. Yang, Y. Guo, Y. Zheng, X. Wang, Q. Yan, Hexagonal-phase cobalt monophosphosulfide for highly efficient overall water splitting, ACS Nano 11 (2017) 11031–11040.
[22] P. Chen, T. Zhou, M. Zhang, Y. Tong, C. Zhong, N. Zhang, L. Zhang, C. Wu, Y. Xie, 3D nitrogen-anion-decorated nickel sulfides for highly efficient overall water splitting, Adv. Mater. 29 (2017), 1701584.
[23] H. Wang, S. Min, C. Ma, Z. Liu, W. Zhang, Q. Wang, D. Li, Y. Li, S. Turner, Y. Han, et al., Synthesis of single-crystal-like nanoporous carbon membranes and their application in overall water splitting, Nat. Commun. 8 (2017) 13592.
[24] F. Hu, S. Zhu, S. Chen, Y. Li, L. Ma, T. Wu, Y. Zhang, C. Wang, C. Liu, X. Yang, L. Song, X. Yang, Y. Xiong, Amorphous Metallic NiFeP: a conductive bulk material achieving high activity for oxygen evolution reaction in both alkaline and acidic media, Adv. Mater. 29 (2017), 1606570.
[25] S.-H. Bae, J.-E. Kim, H. Randriamahazaka, S.-Y. Moon, J.-Y. Park, I.-K. Oh, Seamlessly conductive 3D nanoarchitecture of core-shell Ni-Co nanowire network for highly efficient oxygen evolution, Adv. Energy Mater. 7 (2017), 1601492.
[26] M.-I. Jamesh, Y. Kuang, X. Sun, Constructing earth-abundant 3D nanoarrays for efficient overall water splitting - a review, ChemCatChem (2019), https://doi.org/10.1002/cctc.201801783.
[27] M. Oezaslan, M. Heggen, P. Strasser, Size-dependent morphology of dealloyed bimetallic catalysts: linking the nano to the macro scale, J. Am. Chem. Soc. 134 (2012) 514–524.
[28] P. Strasser, in: W. Vielstich, H.A. Gasteiger, H. Yokokawa (Eds.), Handbook of Fuel Cells: Advances in Electrocatalysis, Materials, Diagnostics and Durability, vol. 5, John Wiley & Sons Ltd., Chichester, West Sussex, UK, 2009, pp. 30–47, 6.
[29] X. Han, X. Wu, C. Zhong, Y. Deng, N. Zhao, W. Hu, $NiCo_2S_4$ nanocrystals anchored on nitrogen-doped carbon nanotubes as a highly efficient bifunctional electrocatalyst for rechargeable zinc-air batteries, Nanomater. Energy 31 (2017) 541–550.
[30] Z. Li, M. Shao, H. An, Z. Wang, S. Xu, M. Wei, D.G. Evans, X. Duan, Fast electrosynthesis of Fe-containing layered double hydroxide arrays toward highly efficient electrocatalytic oxidation reactions, Chem. Sci. 6 (2015) 6624.
[31] W. Ma, R. Ma, C. Wang, J. Liang, X. Liu, K. Zhou, T. Sasaki, A superlattice of alternately stacked Ni–Fe hydroxide nanosheets and graphene for efficient splitting of water, ACS Nano 9 (2015) 1977.
[32] C. Zhang, M. Shao, L. Zhou, Z. Li, K. Xiao, M. Wei, Hierarchical NiFe layered double hydroxide hollow microspheres with highly-efficient behavior toward oxygen evolution reaction, ACS Appl. Mater. Interfaces 8 (2016) 33697.
[33] M.W. Louie, A.T. Bell, An investigation of thin-film Ni–Fe oxide catalysts for the electrochemical evolution of oxygen, J. Am. Chem. Soc. 135 (2013) 12329.
[34] F. Yu, H. Zhou, Y. Huang, J. Sun, F. Qin, J. Bao, W.A. GoddardIII, S. Chen, Z. Ren, High-performance bifunctional porous non-noble metal phosphide catalyst for overall water splitting, Nat. Commun. 9 (2018) 2551.
[35] L. Yu, H. Zhou, J. Sun, I.K. Mishra, D. Luo, F. Yu, Y. Yu, S. Chen, Z. Ren, Amorphous NiFe layered double hydroxide nanosheets decorated on 3D nickel phosphide nanoarrays: a hierarchical core-shell electrocatalyst for efficient oxygen evolution, J. Mater. Chem. 28 (2018) 13619–13623.
[36] T. Zhang, M.-Y. Wu, D.-Y. Yan, J. Mao, H. Liu, W.-B. Hu, X.-W. Du, D.T. Ling, S.-Z. Qiao, Engineering oxygen vacancy on NiO nanorod arrays for alkaline hydrogen evolution, Nanomater. Energy 43 (2018) 103–109.
[37] H. Li, Q. Li, P. Wen, T.B. Williams, S. Adhikari, C. Dun, C. Lu, D. Itanze, L. Jiang, D. L. Carroll, G.L. Donati, P.M. Lundin, Y. Qiu, S.M. Geyer, Colloidal cobalt phosphide nanocrystals as trifunctional electrocatalysts for overall water splitting powered by a zinc–air battery, Adv. Mater. 30 (2018), 1705796.